Physics – Uspekhi **61** (3) 289 – 302 (2018) ©2018 Uspekhi Fizicheskikh Nauk, Russian Academy of Sciences

INSTRUMENTS AND METHODS OF INVESTIGATION

PACS numbers: 71.10.Ca, **71.15.–m**, **71.20.–b**, **72.10.–d**

High-frequency size effect study of the Fermi surface of metals

V A Gasparov

DOI: https://doi.org/10.3367/UFNe.2017.05.038125

Contents

Abstract. **This paper reviews experimental and theoretical work on the study of the Fermi surface of pure metals by the aid of high-frequency size effects. Particular attention is given to little-known new ballistic effects such as the time of flight effect, multichannel size effect, and nonlinear size effect.**

Keywords: Fermi surface of metals, radio-frequency size effect, time-of-flight effect, nonlinear size effect, multichannel surface scattering, pure metals

Devoted to the memory of Vsevolod Feliksovich Gantmakher,
Vitalii Vladimirovich Boiko,
and Robert Huguenin

1. Introduction

The Fermi surfaces (FSs) of the majority of pure metals have been widely investigated since the 1960s [1–13]. The results of these studies are represented in a number of reviews. To date, not only has the topology of FSs been restored, but the basic dimensions of the FSs of pure metals have also measured with high accuracy, making it possible to analytically describe the FSs of the majority of metals. The development of theoretical and numerical methods of constructing the electronic structure of metals, such as the pseudopotential, APW (augmented plane wave), and the KKR (Korringa–Kohn–Rostocker scheme), have made it possible to conduct calculations of the electronic structure of these metals on the basis of the obtained experimental information. In spite of the fact that substantial progress has been made in *ab initio* calculations of the electronic structure of metals, the accuracy of these procedures have proven to be insufficient for the analytical description of FSs in comparison with the experimental accuracy. Therefore, various interpolation methods of calculations of the electronic structure of metals with the fitting of the necessary electron–ion potential based on experimental data were developed [14].

Subsequently, however, primary attention was given to the analysis of the mechanisms of electron scattering in pure metals with the aid of radio-frequency and ballistic effects [10–13]. In this review, we have made an attempt to gather together the existing information about the results of studies of the FSs of metals with the aid of high-frequency size effects (HFSEs) that have not been given in the reviews published earlier [1–9].

The main purpose of this review consists in drawing the attention of specialists to very simple methods that make it possible to investigate the FSs of metals with a high accuracy. Notice that in experiments on HFSEs the radial dimensions of the FSs are measured directly, which substantially simplifies the restoration of the FSs. At the same time, in the case of effects based on quantum oscillations (de Haas–van Alphen (dHvA) effect and Shubnikov–de Haas (SdH) effect), it is the area of the extremal section of the FS that is measured. Furthermore, no very strong magnetic fields or low temperatures are required for experiments on HFSEs, contrary to measurements of quantum oscillations. At the same time, experiments with quantum oscillations in high-temperature superconductors carried out in recent years have shown the enormous potential of these effects for restoring the FSs of metals, so it will be given special attention.

In recent years, there have been widely developed studies of FSs with the aid of angle-resolved photoelectron spectro-

---

V A Gasparov Institute of Solid-State Physics,
Russian Academy of Sciences,
ul. Akademika Osip'yana 2, 142432 Chernogolovka, Moscow region,
Russian Federation
E-mail: vgasparo@issp.ac.ru

Received 15 January 2017, revised 8 May 2017
Uspekhi Fizicheskikh Nauk **188** (3) 311 – 324 (2018)
DOI: https://doi.org/10.3367/UFNr.2017.05.038125
Translated by S N Gorin; edited by A Radzig

scopy (ARPES). These experiments and study procedures have been presented in a whole series of reviews [15–17]; therefore, we consider here only the most interesting and impressive results obtained for high-temperature superconductors, referring the reader to the reviews indicated. Notice only that the accuracy of measurements with the aid of ARPES cannot compete with those provided by the methods of HFSEs and quantum oscillations.

2. Ballistic effects

2.1 Cut-off of cyclotron resonance

To illustrate the HFSE phenomenon, let us examine a plane-parallel single-crystal plate (Fig. 1) of a metal of thickness d with a large mean free path l at the liquid-helium temperature in a magnetic field H parallel to the surface of the plate [18].

The plate is excited by a microwave radiation of high-frequency (HF) field, which penetrates into the metal to depth δ of the skin layer. At sufficiently high frequencies, in a sample of thickness d under conditions that satisfy cyclotron resonance (CR), i.e., $\omega = n\Omega = neH/m^*c$, the absorption of the microwave field experiences oscillations as a function of $1/H$ with the Larmor frequency Ω, with the period of revolution of effective electrons that is a multiple of the period $T = 2\pi/\omega$ of the HF field. Here, m^* is the effective mass of electrons (on the extremal sections of the FS), and $n = 1, 2, 3, \ldots$ are integer numbers.

As a result of CR, resonances appear in the absorption spectrum of the microwave field in the magnetic fields $H_n = m^*\omega c/ne$ with a period $\Delta H^{-1} = e/m^*c\omega$ (Fig. 2).

As can be seen from Fig. 2, cyclotron resonances are observed in the thick samples that decrease in amplitude, become broadened, and pass into sinusoidal oscillations with increasing an order number n of the resonance. At the same time, resonances with $n > 27$ disappear in the case of the thin sample in the region of magnetic fields limited by dashed straight lines. As a result, the cutoff of the cyclotron resonance occurs in the magnetic field H_{cut} at which the diameter of the orbit $2\hbar k = (e/c)\, dH_{\text{cut}}$ is comparable to the thickness of the sample d. In weaker fields, resonances can be seen from the sections with smaller diameter and mass (5 and 6 in curve 2). At the same time, it should be noted that no special features in the cut-off field are observed.

From studies of the position of the cut-off field H_{cut} and of the period of oscillations of the cyclotron resonance depending on the orientation of the magnetic field, the section of the FS of tin in the first Brillouin zone (BZ) in the plane (100) and the anisotropy of the cyclotron mass of electrons $m^*(k)$ in this section have been restored [18, 19]. Subsequently, however, a cutoff of the CR was observed only in indium [20], in spite of the detailed CR studies performed on bismuth [8, 9], aluminum [21], and lead [22].

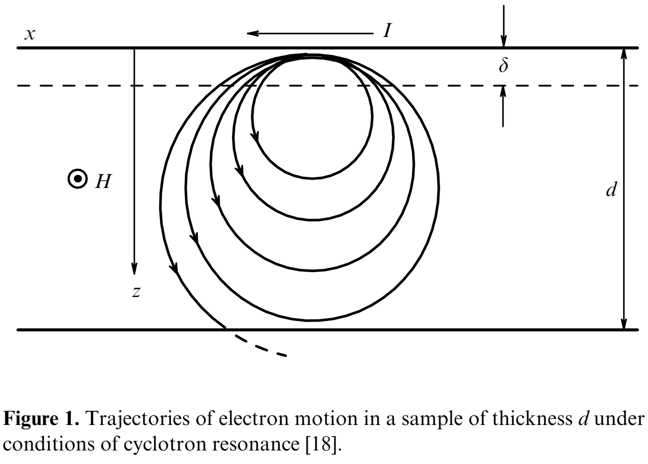

Figure 1. Trajectories of electron motion in a sample of thickness d under conditions of cyclotron resonance [18].

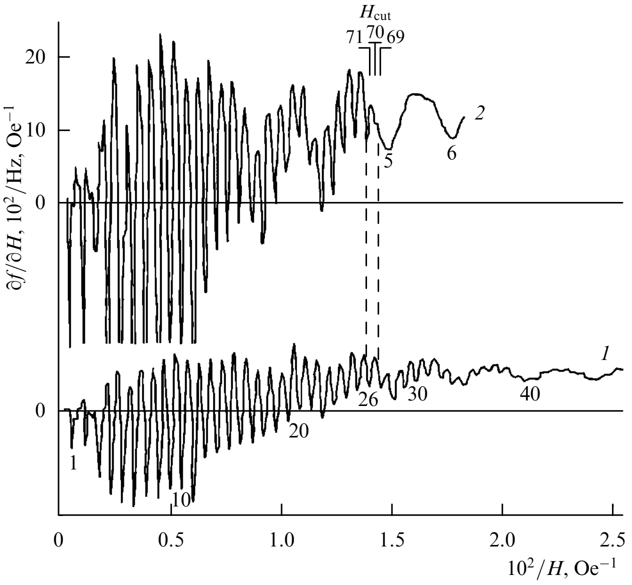

Figure 2. Derivative $\partial f/\partial H$ of the frequency of a strip resonator with respect to the magnetic field recorded on single-crystal tin plates with a thickness of 2 mm (curve 1) and 0.982 mm (curve 2). It can be seen that in the thinner sample the higher-order (27 and above) resonances are cut off (Sn, $T = 3.75$ K, $\omega = 9.4$ GHz, $H \| C_4$, $n \| C_2$) [18]. H_{cut} is a cut-off field of the cyclotron resonance: 69, 70, 71.

2.2 Radio-frequency size effect (Gantmakher effect) in a parallel magnetic field

A true breakthrough in studies of the FSs in metals with the aid of HFSEs was made by V F Gantmakher [23] in experiments using radio frequencies in tin. The studies were carried out under the same conditions as in the work [18, 19] on CR, but at frequencies that were four orders of magnitude smaller (1–5 MHz). No CR was observed at these frequencies. Nevertheless, the depth of the skin layer $\delta \leqslant 10^{-4}$ cm, as before, was much lower in this case than the thickness of the sample. In the magnetic field parallel to the surface of the plate, the electrons move in the bulk of the metal along orbits determined by the individual section of the FS and return into the initial skin layer in the same phase of the electromagnetic field as at the beginning of its path [26]; the frequency of the rotation of electrons along the orbit is considerably greater than the frequency of the RF field ($\Omega \gg \omega$). In this case, on the larger part of the orbit the RF field, which decays in the metal at the depth δ, does not act on them in the zero field, and the electrons obtain an addition to the distribution function in the skin layer.

The density of the RF current in the bursts of the field is rather small, since the contribution to the formation of the lines of the radio-frequency size effect (RFSE) comes from only a small part of different cross sections of the FS. However, near the extremal FS sections the number of such electrons increases substantially; therefore, the current density also increases [26].

From the equation of motion of electrons in the magnetic field with respect to time t,

$$\hbar\dot{\mathbf{k}} = \frac{e}{c}\,[\mathbf{v}\times\mathbf{H}]\,, \tag{1}$$

it can easily be shown [5, 18, 19, 23–27] that the orbits of electrons in the momentum and coordinate spaces are turned relative to each other through the angle $\pi/2$. In this case, the relationship between the diameter $2\hbar k$ of the orbit of electrons in the momentum space and the thickness d of the plate makes it possible to determine the diameter of the section of the FS by the plane perpendicular to H (i.e., the diameter $2\hbar k_{\mathrm{F}}$ of the section of the FS in the momentum space is equal to $(e/c)\,H_0 d$):

$$k_{\mathrm{F}} = \frac{e}{2\hbar c}\,H_0 d\,. \tag{2}$$

Studies of the position of the RFSE lines in the field H_0 depending on the orientation of the magnetic field made it possible to restore the section of the FS of tin in the first Brillouin zone (BZ) [23–26] (Fig. 3b), in excellent agreement with data on the cutoff of the CR [18, 19].

In further experiments, it was discovered that, besides the basic line of the RFSE in the field H_0, lines are observed in fields that are multiples of H_0, i.e., $2H_0$, $3H_0$, etc. In the multiple magnetic fields, the electrons excite the skin layer deep in the metal at a distance that is a multiple of the diameter $\hbar k_{\mathrm{F}}$ of the orbits, when the component v_z of the speed of electrons changes its sign upon reaching the bottom of the orbit [26]. As a result, bursts of the HF field with a phase that is opposite to the phase of the initial skin layer are excited in the bulk of the metal (Fig. 4), with the amplitude of the burst decaying in the depths of the metal. In experiments on Sn [23], the electrons move along the cylindrical section of the FS; therefore, the contribution from different sections reaches its maximum. In the doubled field $2H_0$, the electrons excite a burst of the HF field at a depth of $d/2$, which serves as a source for a new burst in field $3H_0$ at the depth $d/3$, etc. (see Fig. 4). As a result, bursts of the HF field appear at the depth of metal $2r_{\mathrm{extr}} = 2\hbar k_{\mathrm{extr}}/eH$, where it is well screened from the HF excitation in the zero field. The structure of the bursts of the field deep within the metal, $E = E(z)\exp(-\mathrm{i}\omega t)$, is described by the equation [27]

$$\frac{E(n)}{E(0)} = \frac{\Gamma(3/4)}{\pi\sqrt{2}}\,(-1)^n\cos\left(\frac{n\pi}{4}\right)a^n\,\frac{\Gamma(n+1/4)}{\Gamma(n+1)}\,,$$
$$\Gamma(z) = \int_0^1 (-\ln x)^{z-1}\,\mathrm{d}x\,. \tag{3}$$

Here, n is the number of field bursts in a plate of thickness d, δ_0, δ_1, and δ_2 are the depths of the initial skin layer, of the nth burst, and of the burst near the boundary $z = d$, respectively (see Fig. 4) [27], a is the amplitude of the nth burst, and $\Gamma(z)$ is the gamma function.

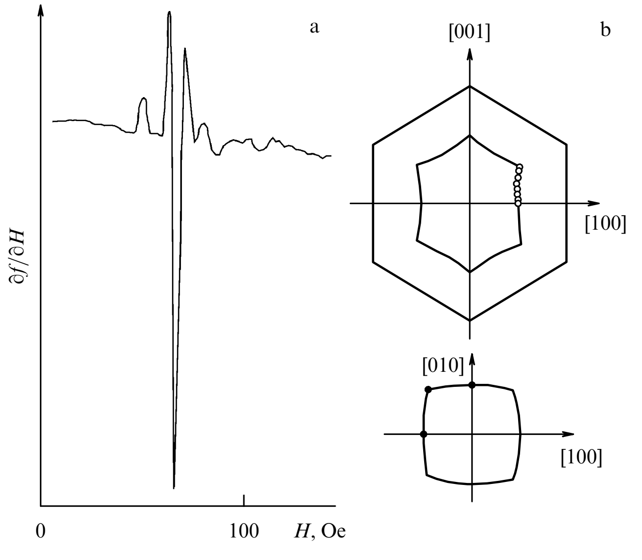

Figure 3. (a) Derivative (with respect to the magnetic field) of the real part of the impedance of a tin sample ($d = 0.54$ mm), recorded at $n\|[100]$, $H\|[001]$, $T = 3.75$ K, and $f = 2.8$ MHz. (b) Cross section of the FS of Sn in the fourth zone in the model of almost free electrons. Points correspond to the results of studies of the RFSE in a parallel magnetic field [23–25].

The amplitude of the HF field in the bulk of the metal by the chain of orbits attenuates rapidly in comparison with the initial amplitude, since the probability of electron scattering grows with increasing n. An example of RFSEs through the chain of orbits in Ag is given in Fig. 5 [29]. In the first approximation, the amplitude of the nth line of the RFSEs is proportional to $n^{-3/4}$ [27]: $A_n \propto n^{-3/4}$.

The amplitude of the basic line of the RFSE in the field H_0 is determined by the probability of electron scattering during orbital movement. Under the conditions of the extremal anomalous skin effect ($l \ll d$), the contribution to the amplitude comes from an exponentially small number of electrons; this makes it possible to study different mechan-

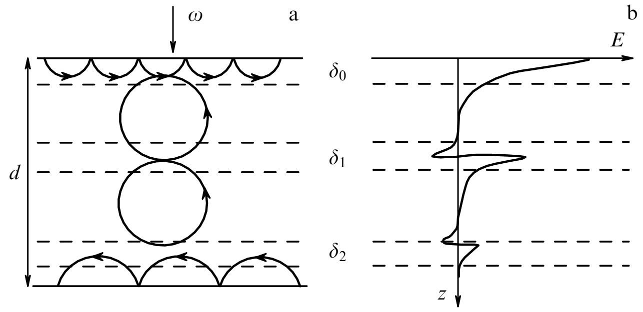

Figure 4. (a) Electron orbits and (b) the distribution of the HF field in the bulk of a metal under RFSEs in multiple magnetic fields [28].

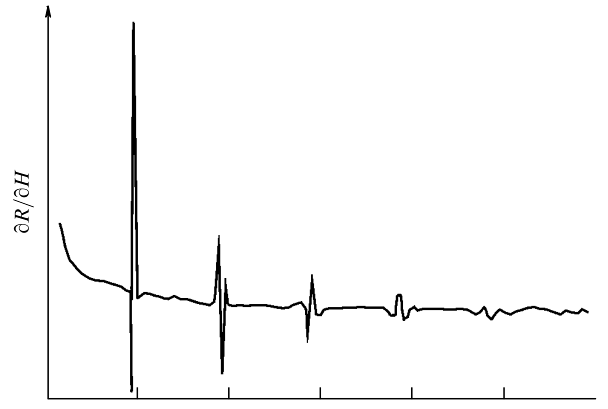

Figure 5. RFSE lines recorded in multiple magnetic fields in Ag ($d = 0.805$ mm, $T = 4.2$ K, $\omega/2\pi = 2.2$ MHz, $n\|\langle 110\rangle$, $H\|\langle 100\rangle$) [29].

isms of scattering and the collision rate $\bar{\nu}(T)$ (electron–phonon, electron–electron, etc.) based on the temperature dependence of the amplitude of the RFSE line [13]:

$$A \propto \exp\left(-\frac{\pi\bar{\nu}}{\Omega}\right). \tag{4}$$

Here, $\bar{\nu}$ is the scattering rate of electrons averaged along the orbit, and Ω is the cyclotron frequency:

$$\bar{\nu} = \frac{\hbar}{2\pi m^*}\oint\frac{\nu(k)\,\mathrm{d}k}{v_\perp(k)}\,. \tag{5}$$

A review of these experiments is published in Ref. [13] and is beyond the scope of this work, where we will be interested only in studies of FSs with the aid of HFSEs.

The value of the field H_0 in formula (2) is determined by the position of the RFSE line, depending on the magnetic field, which is an essential question in calculations of the radial size k_F of the FS. This problem was solved in papers [29, 30] with the aid of the study of the dependence of the position of different extrema of the RFSE lines in In and Mo on the frequency and thickness of the sample, respectively. As follows from Fig. 6, a change in the position of different extrema of the RFSE line depends on the thickness d of the sample in Mo asymmetrically. This circumstance makes it possible to determine the field H_0 in formula (2) based on the left-hand edge of the lines [29, 30], which in turn allows measuring the cross section diameter $2\hbar k$ of the FS with a high accuracy (see Section 2.5).

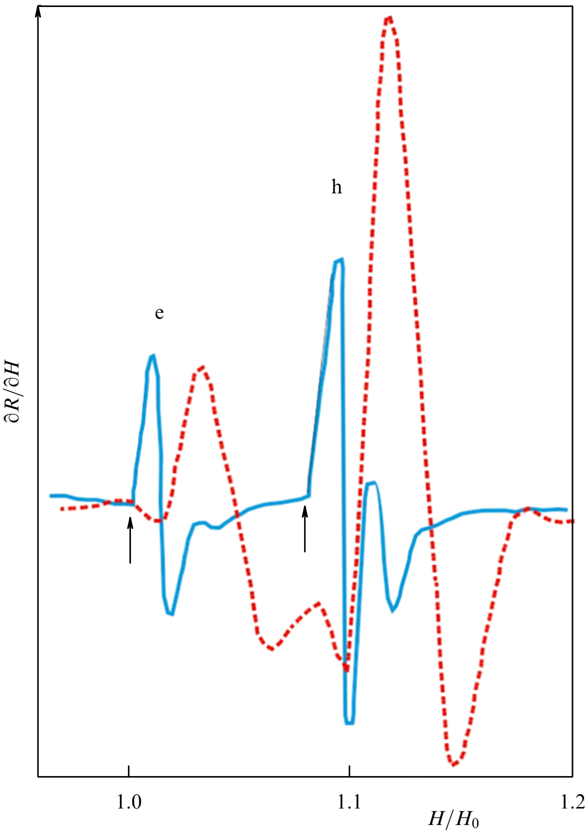

Figure 6. RFSE lines in Mo recorded using samples of various thicknesses: $d = 0.955$ mm (solid curve), and $d = 0.245$ mm (dashed curve). The abscissa axis is normalized with respect to H_0 for the line from the electron jack at Γ (e). The arrows show the positions of the lines for the jack (e) and hole octahedron at H (h) (see Section 2.5) [29].

Similar measurements using rather thick samples of Cu (3 mm) have shown that the sizes of the FS determined based on the left-hand edge agree with the data on the dHvA effect with an accuracy of ±0.2% [29–32].

2.3 Studies of the Fermi surface in Cu and Ag

As an illustration of the potential of the RFSE in a parallel magnetic field for the restoration of FSs, let us examine some results of investigations of this effect in Cu and noble metals (Ag), where the potential of the RFSE for measuring the sizes of FSs manifested itself with a high accuracy [29–32].

The Fermi surface of noble metals is presented schematically in Fig. 7 [34]. This surface is open along the axis ⟨111⟩ and occupies half of the volume of the BZ, whereas in the model of free electrons it takes the form of a sphere inscribed in the BZ. The anisotropy of the positions of the RFSE lines in a parallel magnetic field in the planes (100) and (110) in Ag is illustrated in Fig. 8 [34]. On the ordinate axis, the radius vector of the FS is plotted in units of the radius vector of the

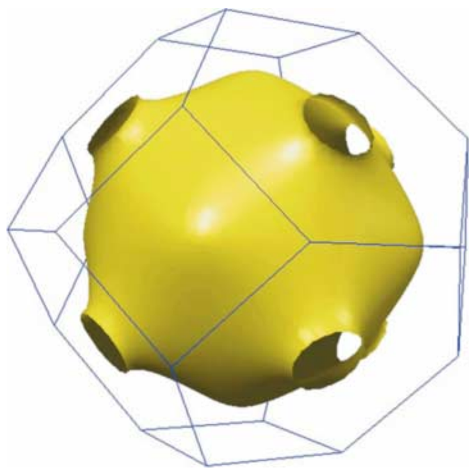

Figure 7. FSs of noble metals (http://www. phys.ufl.edu/fermisurface/).

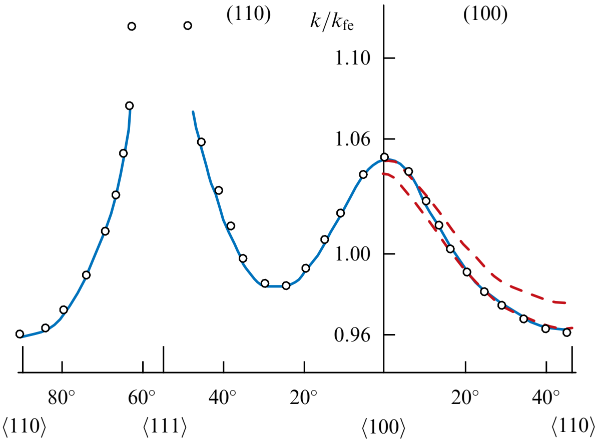

Figure 8. Anisotropy of the positions of RFSE lines in a parallel magnetic field in Ag in planes (110) and (100) [29]. The dashed curves show the results of calculations of the FSs at different values of E_F. The circles correspond to the dHvA data [34], the solid curve to the RFSE results approximated according to formula (6) [29]. The dashed curves in plane (100) correspond to the results of calculations of $k(\theta, \varphi)$ at different values of the Fermi level E_F [35].

sphere of the free electrons $k_{\mathrm{fe}} = 1.2068\ \mathrm{\mathring{A}}^{-1}$ at 4.2 K:

$$k(\theta, \varphi) = (99.58 - 0.16K_1 + 1.63K_2 + 1.36K_3 - 0.53K_4 + 0.03K_5 + 0.29K_6) \times 10^{-3} k_{\mathrm{fe}}\,. \tag{6}$$

The solid curve in Fig. 8 shows the fitting of the $k(\theta, \varphi)$ experimental data in the form of a series in cubic harmonics [29] according to formula (6). Here, k, θ, and φ are the spherical coordinates of a point on the FS. Formula (6) describes the FS with a high accuracy ($\pm 2\%$), except for the region of the neck, which in the experiments on the RFSE in Ag was not observed because of the high scattering rate of electron–phonon collisions in this region of the FS [29, 33].

As can be seen from Fig. 8, the measured sizes of the FS in Ag are in the excellent agreement with the data of the study of the dHvA effect [34], which indicates the high accuracy of the RFSE method. A similar agreement of the data of the RFSE and dHvA effect was demonstrated for Cu [33].

There is a large amount of work in which an attempt was made to describe the FSs of noble metals from the first principles [14]. Nevertheless, as can be seen from Fig. 8, in spite of the wide development of *ab initio* methods, the theoretical models, although describing the shape and sizes of FSs, do not lead to a better agreement with the experiment.

In this sense, a promising method is the utilization of the parametrization of the lattice potential with the fitting of the parameters according to the available experimental data for FSs [14]. Apart from the above-described examples of the employment of the RFSE for studying FSs, numerous studies have been made of the anisotropy of the frequency of both electron–phonon and electron–electron scattering rate, depending on the position at the FS in Cu and Ag [13, 29, 33, 36–38].

2.4 Time-of-flight effect in Ag

Comparatively little attention has been given to another high-frequency size effect — the time-of-flight effect (TFE) [39]. This effect was first discovered in silver in experiments in a parallel magnetic field in the configuration adopted in the RFSE studies, but at four-orders-higher frequencies (45 GHz). In these experiments, a one-sided excitation of an Ag plane-parallel plate was used under conditions of cyclotron resonance. As can be seen from Fig. 9, no CR was observed in a magnetic field higher than the cut-off field H_0, since the diameter of the electron orbit exceeds the thickness d of the sample. However, a microwave signal passing through the sample experiences oscillations, depending on the magnetic field parallel to the sample surface. A theory of this effect was developed in paper [39]. The idea of the TFE consists in the interference of the weak signal of leakage around the sample with the signal having passed through the sample along a ballistic trajectory. As a result of the oscillations of the time of flight relative to the phase of the signal of leakage, an oscillatory dependence of the signal having passed through the sample on the magnetic field appears (see Fig. 9).

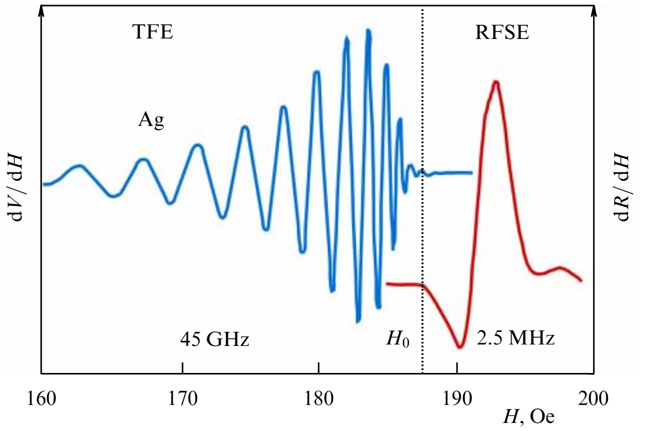

Figure 9. RFSE in silver recorded at 2.5 MHz, and TFE at 45 GHz ($n \| [110]$, $H \| [001]$, $d = 0.811$ mm) [38, 39].

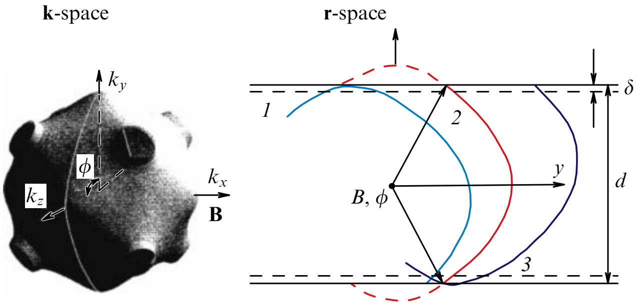

Figure 10. Orbits of electrons in the **k** and **r** spaces that make a contribution to the TFE in Ag. The magnetic field is parallel to the surface of the plate and to the $\langle 100 \rangle$ axis.

As follows from Fig. 9, the position of the RFSE line in the field H_0 determined according to the left-hand edge agrees well with the cut-off field H_0 of the TFE, in accordance with the frequency dependence of the RFSE extrema in In [30] and with the dependence on the thickness of the sample in Mo [31]. As was shown by V F Gantmakher et al. [40], the main contribution to the TFE comes from type *2* orbits (Fig. 10), for which the time of motion in the skin layer (δ/r) is a minimum, as opposed to type *1* and *3* orbits, and, correspondingly, the influence of the effect of delay is minimal. The time of motion in orbit *2* can be represented in the following form [40]:

$$t = \frac{2\hbar}{eH} \int_0^{\phi} \frac{k\,\mathrm{d}\phi}{v_\perp \cos\chi}\,. \tag{7}$$

The amplitude of the TFE oscillations is proportional to the number of electrons having passed without scattering along orbit *2*, and takes on the same form as the amplitude of the RFSE line in the parallel magnetic field [formula (5)], with the difference being that $\bar{v}$ has been averaged over a segment of orbit *2* rather than over the entire orbit, as in the case of the RFSE [41, 42]:

$$\bar{v} = \int_0^{\phi} \frac{v(k)\,k\,\mathrm{d}\phi}{v_\perp(k)\cos\chi} \left(\int_0^{\phi} \frac{k\,\mathrm{d}\phi}{v_\perp(k)\cos\chi} \right)^{-1}. \tag{8}$$

Here, χ is the angle between $v_\perp$ and k, and ϕ is the angle of the start of motion from the surface. Expression (8) contains information about the velocity of electrons averaged over orbit *2*, which makes it possible to restore the Fermi velocity $v(k)$ on the FS from the position of the oscillations of the signal passed through the sample, depending on H [39, 40]. It can be shown [39, 40] that the connection between the Fermi velocity $v(k)$ of electrons and the experimental dependences of the position of TFE oscillations is determined by the following formula

$$v_x = \frac{\omega D}{H(\mathrm{d}\phi/\mathrm{d}H) + \phi}\,, \tag{9}$$

where $\phi = \omega t$. In fact, only a change in the phase $\Delta\phi(H)$ is measured in the experiments, where the phase $\phi(H_c) = \pi H_c/H_0$ is determined by the cyclotron mass known from the CR ($H_c = \omega m^* c/e$), H_0 is the field of the TFE cut-off, and D is the diameter of the orbit in the momentum space. As a result, we obtain

$$\phi = \Delta\phi(H) - \Delta\phi(H_e) + \frac{\pi H_c}{H_e}\,. \tag{10}$$

Formula (8) makes it possible to determine the local frequency of $\nu(k)$ electron–phonon collisions [41, 42] with the aid of relationship (7) for the time of flight of electrons [39, 40]:

$$t(H) = \frac{2\hbar}{eH}\int_0^{k_y}\frac{\mathrm{d}k}{v_x}\,, \quad k_y = \frac{eHD}{2\hbar c}\,. \tag{11}$$

In reality, the accuracy of this calculation procedure for the frequency $\nu(k)$ and for the velocity $v(k)$ is somewhat limited because of the presence of different corrections [40], and also because of the insufficient accuracy of the FS model necessary for the calculations. At the same time, the TFE proved to be a sufficiently efficient method for restoring the velocity of electrons [39, 40] and the frequency of electron–phonon collisions on the FS of Ag [41, 42].

2.5 Studies of the Fermi surface of transition metals Mo and W

Another example of a successful application of the RFSE for restoring the FSs of metals are studies of the metals of the chromium group (Mo, W) [31, 32, 45–52].

Figure 11 shows the Lomer model of the FS for these metals [43, 44]. The electron surface consists of an electron jack at the point Γ of the Brillouin zone, at the corners of which the six electron spheroids are located. The hole surface consists of an octahedron at the point H and six ellipsoids at the points N (green curves in Fig. 12). Inside the necks between the jack and the spheroid parts of the FS in Mo are small electron pockets, which are absent in W.

Figure 12a, b displays polar diagrams of the extremal sizes of the FS in Mo restored from the anisotropy of the positions of the RFSE lines in the plane (110) [31, 32, 45–52]. The wave vector k is laid off along the radius in units of $k_0 = 2\pi/a = 1.998$ Å^{-1} (the size of the BZ along the [100] axis). Here, $a = 3.144$ Å is the lattice parameter of Mo at liquid-helium temperatures.

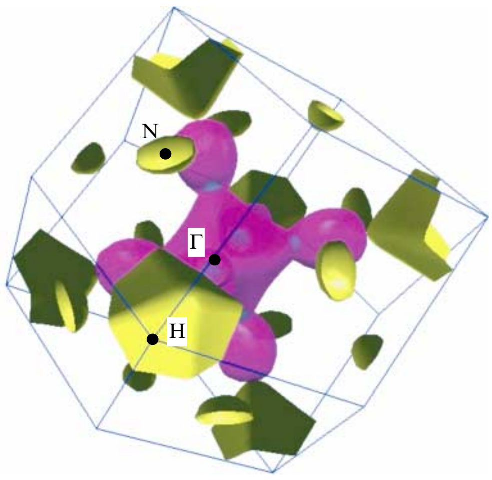

Figure 11. (Color online.) Fermi surface of chromium-group metals (http:www.phys.ufl.edu/fermisurface/).

The position of the lines in the field H_0 was determined from the left-hand edges of the lines [31]. The error in measurements did not exceed 1%. At the same time, the presence of a large number of closely spaced lines, which intersected with the lines in multiple magnetic fields, strongly impeded their identification for different sections of the FSs. Nevertheless, all the RFSE lines turned out to be identified [31, 32, 45–52].

(1) Hole octahedron at the point H. As can be seen from Fig 12a, the h sections well describe the shape of the section of the hole octahedron of the FS in Mo with the symmetry center at the point H of the BZ (see Fig. 11). This circumstance made it possible to determine all the main dimensions of the hole octahedron in Mo: the area of the surface $S = 5.0$ Å^{-2}, and the volume $V = 0.61$ Å^{-3} [47, 48].

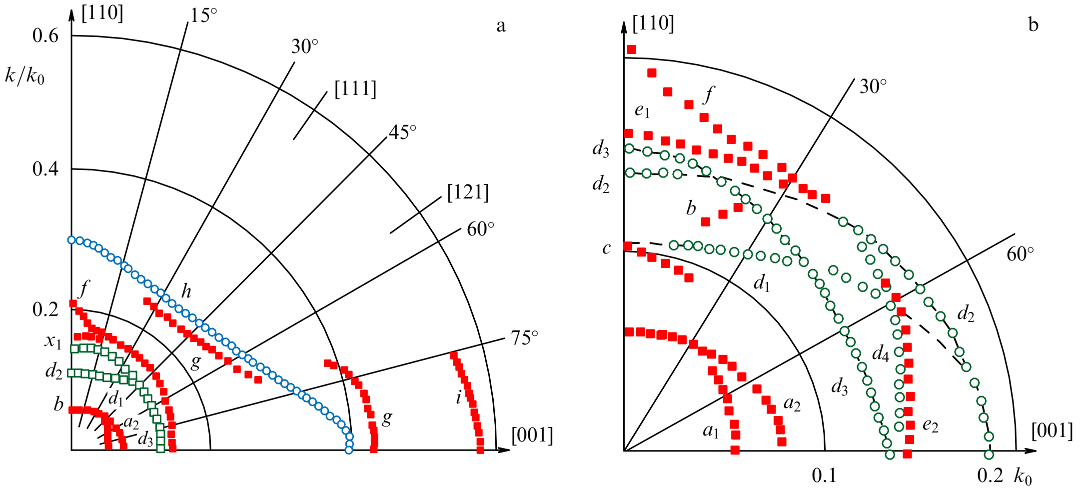

Figure 12. (Color online.) (a) Angular dependences of the wave vector k/k_0 ($k_0 = 2\pi/a$, $a = 1.998$ Å) in the plane (110) in Mo [31, 32, 42, 45–53]. The red points (black squares) correspond to the sections from the electron surface (e); blue dots (light circles) to hole sheets of the FS (h); green points (light squares) to hole ellipsoids (d_1–d_3). (b) Same as in figure (a) but at small k_F.

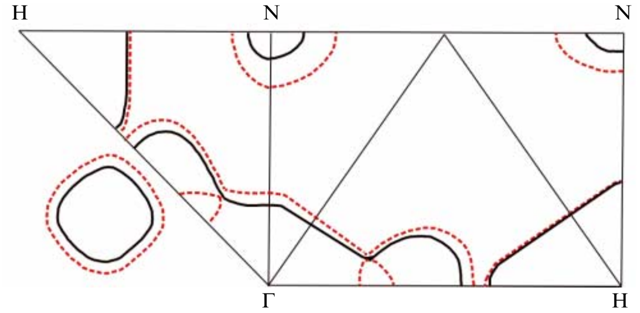

Figure 13. Empirical model of the FS in W (solid lines) and Mo (dotted lines) [48]. An analysis of the positions of these lines made it possible to describe the sections of the FS in W and Mo with a high accuracy [31, 42, 48].

(2) Hole ellipsoids at the point N. Sections d_1, d_2, and d_3 in Fig 12b well describe the sections of the hole ellipsoids at the points N of the BZ. The ellipsoids are elongated along the [100] axis and are compressed along [110]. Investigations in different planes — (100), (110), (111), and (121) — made it possible to determine the dimensions of the principal semiaxes a, b, and c of these ellipsoids with a high accuracy owing to the use of relatively thick Mo samples [31, 47, 48]. The total area of the surface of the ellipsoids is $S = 6.6$ Å^{-2}; their volume is $V = 0.61$ Å^{-3}.

(3) Electron jack at the point Γ and electron lenses. Sections i and g primarily refer to the FS sections on this sheet (Fig. 12a). Apart from these lines, the following lines were also observed: e, spheroids; b, necks on the jack; f, orbits passing through two necks and the octahedral part of the jack.

Section y is due to the bend in the orbit i. This made it possible to determine the distance from Γ to the plane of the neck [48]. The sections a_1 and a_2 of the neck well describe the cone elongated along the [100] axis with a rounded base and an apex. The anisotropy of the position of the lines e_1 and e_2 makes it possible to relate them to electron spheroids. The radius of the spheroids is determined by the section e_1 along the [001] axis with a radius vector equal to 0.32 Å^{-1}. Lines c and b are due to bends in the orbits of the electron jack [31, 47, 48].

(4) Angular range of the existence of lines b and their anisotropy make it possible to relate them to the orbits on the neck of the jack connecting the octahedral part of the jack body with the spheroids. An empirical model of the FSs in W and Mo [48] restored from experiments on the RFSE in the parallel magnetic field is shown in Fig. 13. An analysis of the positions of these lines made it possible to describe the sections of the FSs in W and Mo with a high accuracy [31, 47, 48].

2.6 Radio-frequency size effect in tilted and perpendicular magnetic fields

As was already noted above, the RFSE in a parallel magnetic field is due to 'effective electrons', which move in the skin layer parallel to the surface with a velocity $v_z = 0$. Another example of effective electrons is the RFSE at the limiting point or at the section of the FS with an extremal derivative of the surface area of the section with respect to the momentum, $\partial S/\partial k_z$ [5, 13, 30, 51–54, 56]. In this case, the electrons start moving parallel to the surface in the skin layer and continue moving deep in the metal in spiral orbits (Fig. 14) [13, 27, 30].

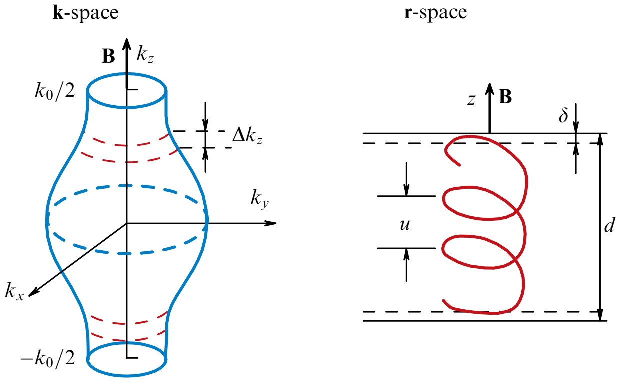

Figure 14. Orbits of electrons in the **k** and **r** spaces for the corrugated FS that are responsible for the GKO effect in the magnetic field perpendicular to the sample surface [13].

The extremal shift of electrons deep to the metal (u) depending on the electron momentum k_z along the magnetic field can take place for the orbit at the elliptic limiting point [30, 54, 56]:

$$u_0 = \frac{2\pi c}{eHK^{1/2}}\,, \tag{12}$$

where K is the Gaussian curvature of the FS at the limiting point.

For an arbitrary FS, such extrema can occur at the noncentral sections of the FS with an extremum of $\partial S/\partial k_z$ (see Fig. 14) [5, 13, 30, 54–58]:

$$u_1 = \frac{c}{eH\hbar}\left|\frac{\partial S}{\partial k_z}\right|, \tag{13}$$

where $S(k_z)$ is the area of the section of the FS with the plane $k_z = \mathrm{const}$.

The electron motion in such an orbit in a parallel magnetic field leads to a shift in the position of the RFSE lines according to the law: $H = H_0 \cos\varphi$ for the RFSE from the orbits at the noncentral section of the FS [30, 54, 55]. Here, φ is the tilt angle of the field, and H_0 is the position of the RFSE line in the parallel magnetic field. For electrons at the noncentral sections of the FS in a tilted field, a drift component $v_H\varphi$ of the velocity oriented along the normal to the surface **n** appears. It can be shown that the diameter D of the spiral orbit is related to the plate thickness d according to the formula [54–56]

$$d = D\cos\varphi + \left(n - \frac{1}{2}\right)h\sin\varphi\,, \quad n = 0, 1, 2, \ldots\,. \tag{14}$$

Here, D is the diameter, and h is the pitch of the spiral orbit.

The RFSE in the case of orbits at the limiting point or at the noncentral section of the FS takes place at those values H_n of the magnetic field for which the number n of rotations along the path from one side of the sample to the other side is an integer. As a result, RFSE lines were observed at the limiting point in In for the direction of the magnetic field along [111], which were periodic with respect to the field [30, 54–56]:

$$\Delta H = H_n - H_{n-1} = \frac{2\pi c}{ed}\,K^{-1/2}\varphi\,. \tag{15}$$

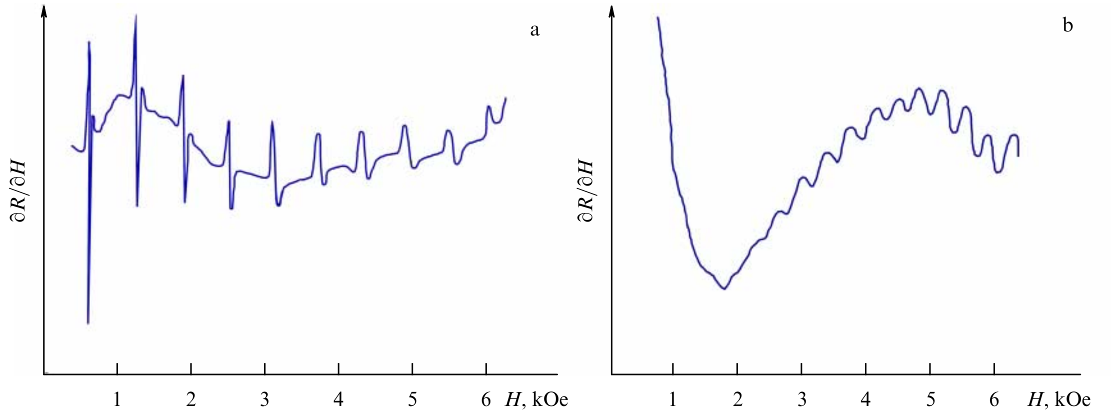

Figure 15. RFSE lines recorded in a tilted magnetic field in Mo and caused by the orbits on a hole octahedron at the point H of the BZ with an extremal derivative $\mathrm{d}S/\mathrm{d}k_z$ [48]. Tilt of the magnetic field in the plane ([110], n), $d = 0.245$ mm, $f = 3.5$ MHz, and $T = 4.2$ K. (b) RFSE lines recorded from the noncentral sections on the hole octahedron in Mo in a perpendicular magnetic field ($n \| [110]$, $f = 3.5$ MHz, $T = 4.2$ K, $d = 0.239$ mm) [48].

The period ΔH in the position of the lines made it possible to determine the Gaussian curvature K of the FS in In at the limiting point [30, 54].

The RFSE in the case of the noncentral sections of a hole octahedron with an extremal derivative $\partial S/\partial k_z$ was observed in Mo and W [48] (Figs 15a, 15b). The same effect is responsible for the splitting of lines in W in a tilted magnetic field [48]. However, the variety of RFSEs is not only due to the narrow character of the lines in a parallel or tilted magnetic field.

As follows from Fig. 15b, harmonic oscillations of the derivative of the surface impedance in Mo, in a magnetic field perpendicular to the surface, are observed with respect to the magnetic field [48]. Similar oscillations were observed in a perpendicular field in Sn [57] and Cd [58–60]. This effect is known as the Gantmakher–Kaner effect [56] and is due to the existence of ineffective electrons with a nonzero component v_z of the velocity along the normal **n** (see Fig. 14). The excitation of electrons by a microwave field is the same, irrespective of the orbit, for those harmonics of the microwave field in metal, for which the wavelength $\lambda_n = u/n$ ($n = 1, 2, 3, \ldots$) is a multiple of the shift u of the electrons into the metal per cyclotron period [56].

This circumstance leads to a harmonic distribution of the microwave field in the metal, contrary to the case of geometrical resonances considered above for the cases of parallel and tilted magnetic fields. In the harmonic case, the metal becomes transparent to the electromagnetic excitation. The period of Gantmakher–Kaner oscillations (GKOs) is determined by the extremum of the displacement u_1, just as in the case of the RFSE in a tilted magnetic field (13), which made it possible to determine such an important characteristic of the FS as the angular dependence of the derivative $|\partial S/\partial k_z|$ from experiments in both the tilted and perpendicular magnetic fields in Mo [48].

2.7 Multichannel radio-frequency size effect in W

Up to now, we have considered the RFSE in the case of a 'normal' scattering of electrons from the surface of the metal, when the electron remains on the same sheet of the FS after surface scattering. However, the law of momentum conservation upon surface scattering requires the conservation only of the tangential component $k_{\|} = \mathbf{kn}$ of the wave vector of electrons, where **n** is the normal to the surface of the sample. Therefore, as follows from Fig. 16, collisions in the case of a multisheet FS can occur with a transfer between the different sheets of the FS or even between different BZs (umklapp scattering). Such a character of the surface scattering was considered theoretically in a whole number of studies [28, 61–65].

If the plane of the orbit lies near the limiting point of the sheet of the FS, then the electrons moving along the jumping trajectories from A to B on the electron jack (see Fig. 16) can experience not only conventional specular scattering to point B but also perform jumps to points C and D on the same sheet of the FS with the same $k_{\|}$. Such electrons can continue moving in the jumping orbit and even jump onto a hole sheet of the FS (see Fig. 16). As a result, a hole can appear with a larger diameter of the orbit and, correspondingly, a new RFSE line will arise. The probability of the jumps is proportional to the angle of scattering φ [63–65]:

$$p_{\mathrm{BC}} = \alpha_{\mathrm{BC}}(k_{\|})\, v_{\mathrm{B}}(k_{\|})\, v_{\mathrm{C}}(k_{\|}) = a_{\mathrm{BC}}(k)\, \varphi\,. \tag{16}$$

Here, α_{BC} depends on the wave functions of electrons at the points B and C, and v_{B} and v_{C} are the normal components of the electron velocities at these points. As can be seen from

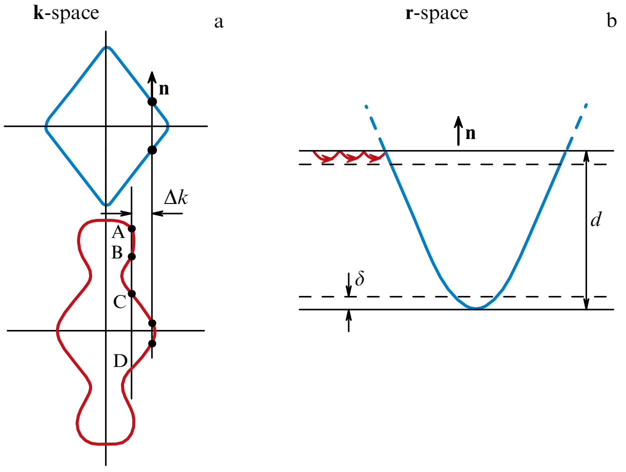

Figure 16. Multichannel surface scattering of electrons in the **k** and **r** spaces in W and Mo.

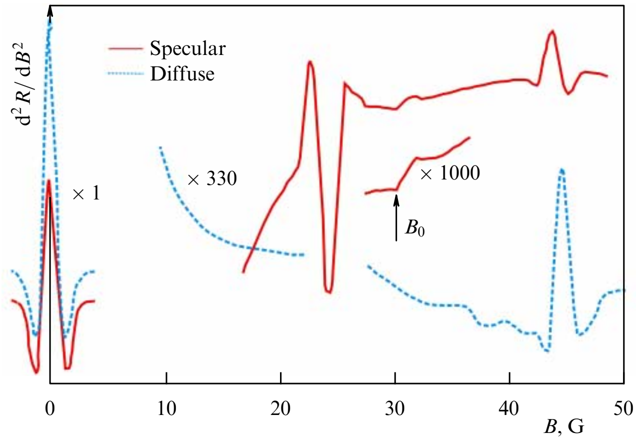

Figure 17. RFSE lines recorded in a W sample with a specular (solid lines) and diffuse (dotted lines) surface, $H||[100]$, $d = 0.43$ mm, $\omega/2\pi = 1.9$ MHz, and $T = 1.35$ K.

Fig. 16, there are a large number of possible channels in W and Mo for multichannel surface scattering.

We observed this type of RFSE in a parallel magnetic field in W samples with a mirror-finish surface [66]. Any of these jumps can lead to the appearance of new RFSE lines in different magnetic fields, which are not observed in samples with a diffuse surface.

As can be seen from Fig. 17, besides the lines investigated earlier [47], a new line was observed in the magnetic field of 30 Oe, which disappears after etching the surface of the sample. At least two new RFSE lines were also observed in the experiments at $H||[100]$, which were caused by different types of jumps of holes jumping onto the electron spheroid and back, and also of electrons jumping onto the spheroid in an adjacent BZ [66]. The position of these lines agrees well with the jumps upon multichannel scattering. A change in the frequency did not affect the position of these lines. They disappeared upon a change in the orientation of the magnetic field by several degrees relative to the optimum orientations. The decrease in the thickness of the sample led to the displacement of these lines into the range of stronger fields, together with the basic lines of the RFSE (dashed curves in Fig. 17) [66]. The amplitude of these lines is approximately an order of magnitude lower than the amplitude of conventional lines in closed orbits because of the small probability of specular scattering with a jump for the jumping orbits, which is proportional to the incidence angle [formula (16)].

Apparently, it is because of the small probability of the surface scattering that the latter was not discovered in experiments on electron focusing in the transverse magnetic field in W [67]. This method is very efficient for the observation of the specular reflection of electrons in metals [68].

2.8 Nonlinear radio-frequency size effect in Bi

So far, we have considered the RFSE under linear conditions, when the amplitude H_ω of the microwave field at the surface of a sample is small compared to an external constant magnetic field H_0. In this case, the electron orbits are not distorted in the skin layer. The situation changes substantially in the case of the reverse limit, when $H_\omega \geqslant H_0$ [69, 70]. Under these conditions, the magnetic field of a wave superimposed on H_0 leads to the nonequivalence of two half-periods of the alternating current in the skin layer. As a result, a DC component of the microwave current arises near the surface. This current attenuates at the depth δ but is carried into the depths of the sample in the form of antisymmetric bursts of the direct current with an alternating sign, just like bursts of the HF current in the RFSE through the chain of orbits (see Section 2.2, Fig. 4).

The amplitude of the bursts diminishes with the order number n according to the law $n^{-2/3}$, almost just as the bursts of the HF field decrease [formula (3)]. The magnetic field of the rectified current acts on the orbits of the electrons together with an external magnetic field. As the external field reaches the strength $H_n = 2nvmcled$, where d is the thickness of the plate, and n is an integer, the bursts of the direct current go onto the opposite surface of the sample and can be detected based on the dependence of the magnetic moment of the sample on the external magnetic field [69–71].

The RFSE under nonlinear conditions was observed in Bi [70, 71] based on the dependence of the derivative dM/dH of the magnetic moment of the sample on the strength of the DC magnetic field parallel to the surface of the sample (Fig. 18). The fact is that the FS of the semimetallic Bi consists of three electron sheets and one hole sheet close in shape to ellipsoids with anomalously small sizes in comparison with the metals examined above (see inset to Fig. 18). Therefore, the linear RFSE is observed in a very weak magnetic field of 1–2 Oe. At larger amplitudes of the HF field, from 0.5 to 6 Oe, a nonlinear RFSE was observed from the dependence of the derivative dM/dH on H, when the condition $H_\omega \propto H_0$ of the nonlinearity was satisfied.

Figure 18 depicts an example of a record of the nonlinear RFSE in Bi [69, 70]. It can be seen that the left-hand edge of the nonlinear RFSE (curve *2*) is displaced into the range of weak fields because of the presence in the sample of a constant magnetic field created by the rectified current. This displacement increased with increasing H_ω, in accordance with the theory suggested in Refs [70, 71]. Furthermore, lines of the nonlinear RFSE were observed in multiple magnetic fields [70, 71].

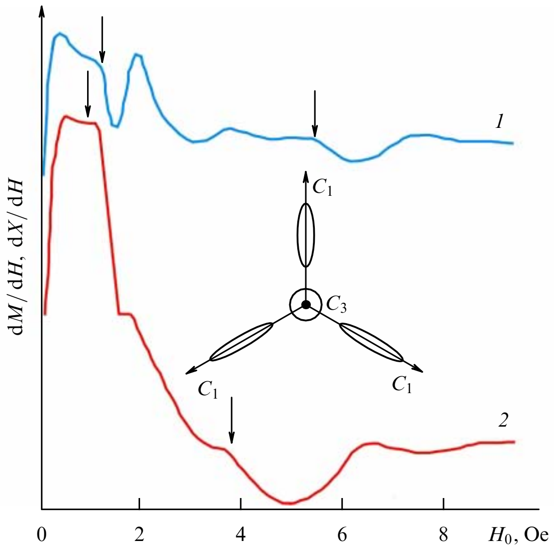

Figure 18. Profiles of (*1*) linear and (*2*) nonlinear radio-frequency size effects in Bi. Amplitude of the HF field is $H_\omega = 0.1$ Oe. The arrows indicate the left-hand edges of the lines. The constant magnetic field is directed at the angle of 13° toward the axis C_2; $n||C_3$; $d = 0.58$ mm [70, 71].

At large amplitudes of the electromagnetic field, the rectified current may not disappear after the switching off the magnetic field, since it proves to be sufficient for the rectification. In other words, this means that in a metal plate upon excitation by an electromagnetic field with a large amplitude the 'current' states, i.e., states in which a closed direct current flows in the sample, can be implemented even in the absence of an external magnetic field [70–75].

An interpretation of the results of investigations into current states in different metals [70, 71] is presented in detail in review [71]; it is beyond the scope of this review, which is devoted to the fermiology of metals.

3. De Haas–van Alphen effect

3.1 Quantum oscillations in ZrB_{12}

As has already been noted in the Introduction, the other most popular effects for the study of FSs in metals are the quantum oscillations of magnetic susceptibility (de Haas–van Alphen effect) and of the conductivity of metals (Shubnikov–de Haas effect). In these effects, the area of the extremal sections of the FSs is measured, which substantially complicates the restoration of the FSs. Nevertheless, we consider below a number of results obtained recently in the case of high-temperature superconductors, without claiming that the information available on this enormous subject is complete [1, 2, 10].

As is known from the theory of the electronic structure of metals [76], part of the energy of electrons connected with motion in the plane perpendicular to the magnetic field is quantized in strong magnetic fields. In the quasiclassical case, the Lifshits–Onsager quantization condition takes on the following form [76]:

$$S(\varepsilon, p_z) = \frac{2\pi\hbar e H}{c}\,(n+\gamma)\,, \quad n = 0, 1, 2, \ldots\,. \tag{17}$$

Here, H is the strength of the magnetic field along the z-axis; $S(\varepsilon, p_z)$ is the area of the section of the FS by the plane $p_z = \text{const}$ perpendicular to H; $\gamma = 1/2$, and e is the electron charge. The quantization of the electron energy leads to oscillations of the magnetic susceptibility $\tilde{M}_{||}$ and of the conductivity of metals in the reversed magnetic field $1/H$, which makes it possible to determine the area of the extremal sections of the FSs:

$$S_{\text{extr}} = \frac{2\pi\hbar e}{c\Delta H^{-1}}\,. \tag{18}$$

The frequency of the oscillations of the parallel magnetization $\tilde{M}_{||}$ is proportional to the surface area S_{F} of the corresponding sheet of the FS: $F = (S_{\text{F}}\hbar c)/2\pi e$. In metals, the amplitude of oscillations $A(T, H)$ is described by the Lifshits–Kosevich formula [76]:

$$A \propto H^{1/2}\left|\frac{\partial^2 S_{\text{F}}}{\partial k^2}\right|^{-1/2} \frac{\alpha m_{\text{c}} T/H}{\sinh\left(\alpha m_{\text{c}} T/H\right)} \exp\left(-\frac{\alpha m_{\text{c}} T_{\text{D}}}{H}\right), \tag{19}$$

$$\alpha = \frac{2\pi^2 c k_{\text{B}} m_0}{e\hbar} = 14.693\, T_{\text{D}}\,[\text{K}]\,.$$

Here, $m_{\text{c}} = \hbar^2(\partial^2 E_{\text{F}}/\partial k^2)/2\pi$ is the cyclotron effective mass of electrons, and $T_{\text{D}} = \hbar/2\pi k_{\text{B}}\tau$ is the Dingle temperature, which is inversely proportional to the frequency τ of electron collisions.

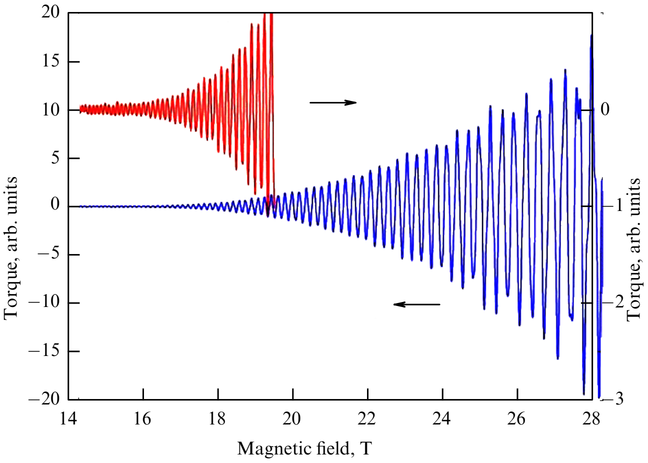

Figure 19. Typical example of dHvA oscillations in ZrB_{12} single crystals in a magnetic field oriented along the $\langle 110 \rangle$ axis [77].

Formula (19) makes it possible to determine the frequency of oscillations and, correspondingly, the area (18) of the extremal section of the FS. As an example of studies of the dHvA effect, the quantum oscillations in ZrB_{12} are displayed in Fig. 19 [77]. Notice that the β and ε peaks in the Fourier expansion (Fig. 20) appear only in strong magnetic fields because of the magnetic breakdown of the 'dog's bone' and 'cubic box' type orbits (see inset to Fig. 20).

The solid curves in Fig. 21 demonstrate a close agreement between the experiments and *ab initio* calculations of the energy-band electronic structure of ZrB_{12}. The theoretical model of the FS in ZrB_{12} is shown in Fig. 22 for the hole and electron sheets of the FS. The red curves in Fig. 22 depict the orbits on the 'neck' and on the 'cubic box'. The minimum frequency on the α-branch, between $1.2kT$ and $2kT$, corresponds to the orbits on the neck of the FS (orbit N in Fig. 22). The branches near $6kT$ (see Fig. 20) are caused by the 'cubic-box' electron orbits. As a result of the conducted investigations, it was possible to identify all sections of the FS in ZrB_{12}. Some discrepancy between the experiment and calculations is caused by the imperfection of the theoretical

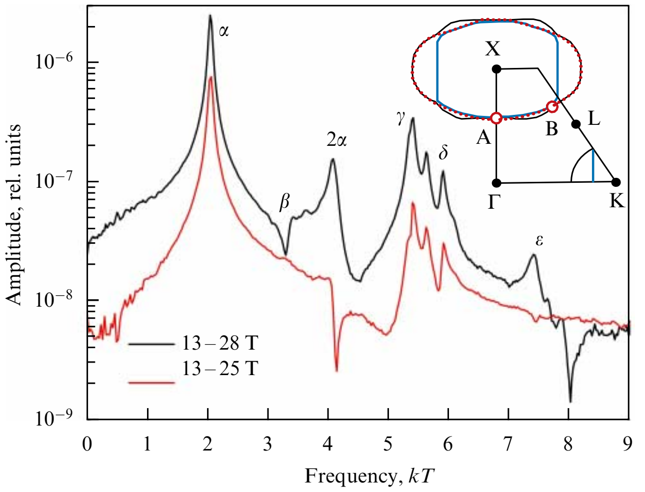

Figure 20. Fourier expansion of quantum oscillations in ZrB_{12} for a magnetic field directed along the $\langle 110 \rangle$ axis [77]. In the inset, the 'cubic-box' type orbit is shown.

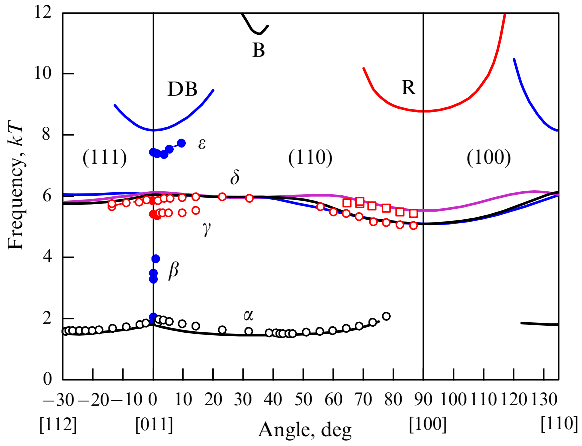

Figure 21. Experimental results (points) for the anisotropy of the frequency of dHvA oscillations and the theoretical curves, which correspond to extremal orbits on the FSs of ZrB_{12}: 'dog's bone' (DB), 'belly' (B), and 'rosette' (R), respectively. The solid curve is the result of calculations for $E_F = 0.16$ eV [77].

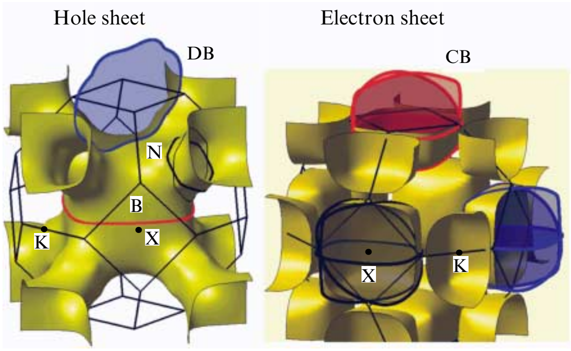

Figure 22. (Color online.) Hole and electron sheets of the FS in the theoretical model of the FS of ZrB_{12} [77]. Here, DB and CB designate 'dog's bone' and 'cubic box' type orbits.

model, just as, strictly speaking, in the case of the FS of Ag [29] (see Section 2.3).

The dHvA effect in the extremal case, when $4\pi[(dM/dH) - 1] > 1$, leads to the formation of diamagnetic domains [78]. But this is the topic of a separate review [79].

The above results demonstrate the advantage of the experimental methods above the calculations of the electronic structure of metals for the restoration of FSs, which has already been discussed above (see Section 2.3).

3.2 Quantum oscillations in $YBa_2Cu_3O_{7-x}$

Another example of recent extremely successful studies of FSs in superconductors are quantum oscillations in single crystals of the high-temperature superconductors $YBa_2Cu_3O_{7-x}$ (YBCO) and $HgBa_2CuO_{4+x}$ (HBCO) [80–91]. In them, quantum oscillations of magnetic susceptibility, high-frequency conductivity, magnetic moment, the Hall effect, and the Seebeck and Nernst effects have been detected in a wide range of magnetic fields (20–101 T) and temperatures (1.1–30 K).

Figure 23 presents an example of quantum oscillations of the high-frequency conductivity of a single-crystal YBCO ($x = 0.56$), measured based on the dependence of the frequency of a tunnel-diode generator on the reversed magnetic field [88]. The measurements were conducted using the same procedure as in the measurement of HFSEs, based on the shift in the resonance frequency of an autodyne generator depending on the magnetic field.

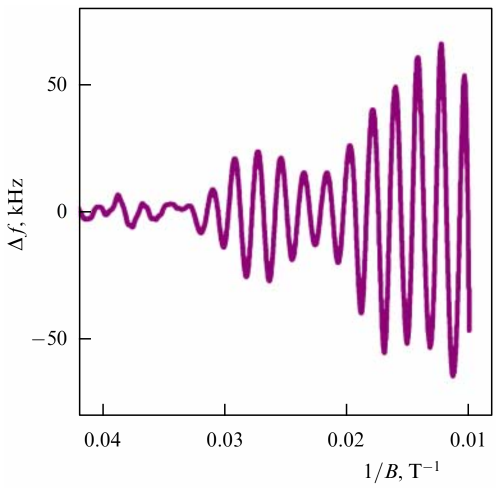

Figure 23. Quantum oscillations in underdoped $YBa_2Cu_3O_{7-x}$ with $x = 0.56$ up to 101 T at $T = 1.5$ K as functions of the reversed magnetic field $1/B$ [88].

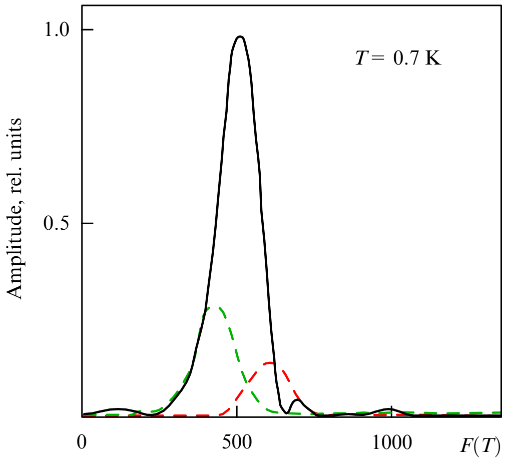

Figure 24. Fourier expansion of quantum oscillations in the single-crystal YBCO (see Fig. 23) [88].

As a result of the investigations conducted, quantum oscillations were discovered up to 30 K, with a frequency which corresponds to small pockets on the FS of the YBCO, with a rather small effective mass $m^* = 0.45m_0$ (see Fig. 23). A Fourier analysis of these oscillations (Fig. 24) showed that they were caused by both electron and hole sheets of the FS. It was established in Refs [80–91] that the FS of the YBCO consists of one electron pocket and two hole pockets in the form of deformed cylinders, in accordance with the reconstruction of the FS caused by charge-density waves (CDWs) [88] (Fig. 25).

It is probable that two of the ellipsoids in Fig. 25 are connected with two different sheets of the FS, which are caused by CuO_2 planes in the unit cell of the YBCO [88]. The third frequency of oscillations in Fig. 24 is possibly due to the magnetic breakdown between the electron and hole ellipsoids

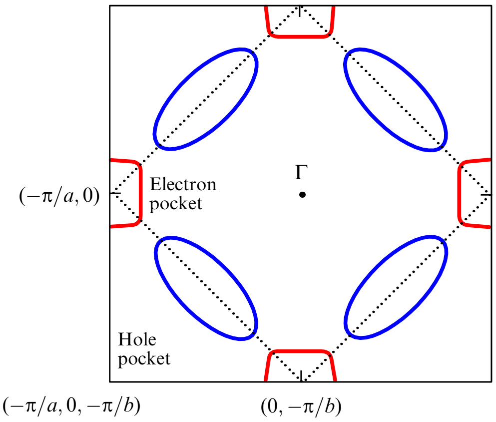

Figure 25. (Color online.) Section of a reconstructed FS of YBCO, which consists of a lozenge-shaped electron pocket (red) and hole ellipsoids (blue) [88]. The dotted lines correspond to the antiferromagnetic Brillouin zone.

of the FS [88], which is very likely in such strong magnetic fields as 20–101 T.

4. Angle-resolved photoelectron spectroscopy

The method of angle-resolved photoelectron spectroscopy (ARPES) occupies a special position among contemporary methods of studies on FSs of metals. A specific feature of this method of study of the electronic structure of metals is the capacity to study low-lying energy levels of metals, located below the Fermi level [15–17].

The ARPES method is based on the phenomenon of the photoeffect. Upon irradiation of the surface of a metal by ultraviolet radiation, the emission of electrons of different energies occurs, which is registered in the form of a photoemission spectrum and, if using a sweeping over the angle, is recorded as an angle-resolved photoemission spectrum (Fig. 26) [15–17].

In the ARPES experiments, the electrons emitted from the surface of the metal fall onto a hemispherical analyzer, whose lens directs the electrons onto special multichannel plates. Upon further flight through the analyzer, the electron beam is swept over energy in the plane perpendicular to the slit, and a two-dimensional spectrum forms on a 2D detector: the intensity of photoelectrons as a function of their energy and the angle of ejection. The sample and the detector are placed in an ultrahigh vacuum, since ARPES is a surface-sensitive method. As the source of irradiation, either synchrotron emission (20–200 eV) or the emission of a helium plasma ($\sim$ 20 eV) is used; recently, modern lasers with a quantum energy of 7 and 11 eV began to be used [15–17].

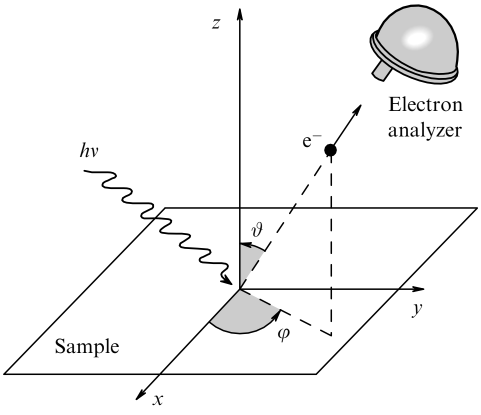

Figure 26. Diagram of an ARPES experiment in which the direction of the electron emission is determined by the angle ϑ and the polar angle φ. The electron emission is registered by an electron analyzer [15].

The ARPES method is based on a not-entirely-substantiated assumption that an electron, when being emitted from a crystal into a vacuum, preserves its momentum and energy; i.e., it is assumed that on leaving the crystal the quasi-momentum $\hbar\mathbf{k}$ of the electron passes into real momentum in a free space: $\mathbf{p} = \hbar\mathbf{k} + \hbar\mathbf{G}$, where $\mathbf{G}$ is the vector of the reciprocal lattice of the crystal. In this case, the energy of the electron is retained: $E_{\text{kin}} = h\nu - \varphi - |E_{\text{b}}|$, where E_{b} is the electron binding energy in the metal.

The intensity of the photocurrent is proportional to the spectral function multiplied by the Fermi distribution function: $I(k,\omega) = A(k,\omega)\,f(\omega)$. Without taking into account the interaction, we have $A(\mathbf{k},\omega) = \delta[\omega - \varepsilon(\mathbf{k})]$, and the electronic spectrum is determined by the law of the energy-band dispersion $\varepsilon(\mathbf{k})$ in the metal. Allowance for the interaction strongly complicates the behavior of the spectral function:

$$A(k,\omega) = -\frac{\Sigma''(\omega)}{\pi\big(\omega - \varepsilon(k) - \Sigma'(\omega)\big)^2 + \Sigma''(\omega)^2}\,.$$

Here, $\Sigma'(\omega) + \mathrm{i}\Sigma''(\omega)$ is the quasiparticle self-energy, which reflects the interactions in the metal. Generally speaking, there has been no strict substantiation of the effect of ARPES to date; therefore, as a rule, different approximations are used [15–17]. It should be noted that ARPES is a surface-sensitive method, since the mean free path of photoelectrons greatly depends on energy, with a minimum at 2–5 Å. Therefore, it is not entirely obvious to which extent the ARPES spectrum reflects the real electronic structure in the bulk of the metal rather than the structure of surface states. Thus, it was shown in Refs [15–17] that the photoemission in cuprates occurs from a depth on the order of two unit cell constants, i.e., $\sim$ 15 Å.

Figure 27 displays a model of the section of the FS of a YBCO single crystal, which consists of pairs of outlines around the point S in the Brillouin zone, corresponding to the connected and anti-connected sheets of the FS, restored with the aid of ARPES by the application of circularly polarized ultraviolet radiation [92]. In these experiments, it was possible to localize the position of surface and bulk states in the YBCO, where the CuO_2 layer nearest to the surface is considered to be localized, and the next bilayer is considered as lying in the bulk.

At present, apparently, there is a fundamental discrepancy between ARPES data for FSs and the results of studying quantum oscillations [77–91]. It should also be noted that studies of quantum oscillations are carried out in strong magnetic fields, whereas ARPES data are obtained in a zero field [77–88]. Nevertheless, it seems that the existing nonconformity requires careful study.

Summarizing the results of the investigations of quantum oscillations and ARPES in the YBCO, note the following circumstances [88]: (1) a sharp decrease of the dimensions of the FS was discovered upon going over from the underdoped to overdoped regime and a rapid decrease in the Fermi

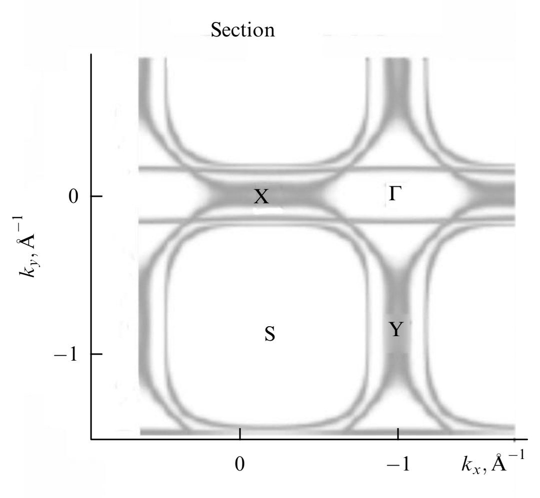

Figure 27. Electron-band structure of a de-twinned single crystal of $YBa_2Cu_3O_{6.85}$ [92].

velocity in the case of low doping; (2) ARPES reveals the transformation (collapse) of the large FS on the overdoped side into unconnected arcs of the FS; (3) quantum oscillations are explained by the magnetic breakdown between the hole and electron pockets of the FS.

Note in conclusion that investigations of the FS in $YBa_2Cu_3O_{7-x}$ are beyond the scope of this review, which is devoted to the fermiology of pure metals. Nevertheless, a number of the above results show the undoubted importance of these studies for obtaining information about the electronic structure of metals.

5. Conclusion

In this review, we undertook an attempt to gather together the results of studies of the Fermi surface of metals performed with the aid of high-frequency size effects. We have shown the high accuracy of these methods using examples of studies that did not enter into other reviews. We have shown that high-frequency size effects are very sensitive and efficient methods for studying FSs and mechanisms of the excitation of electromagnetic waves in metals. Unfortunately, such studies are presently absent because of the necessity of using high-purity metals with a large mean free path of electrons. At the same time, the application of HFSEs for studies of the FSs of nanostructured objects with a thickness of several micrometers can prove to be very efficient and useful.

It has been shown with the example of the electronic structure of high-temperature superconductors that investigations into the FSs of metals are a very important and fascinating problem in the study of the electronic structure of metals.

Acknowledgments

The author is grateful to V T Dolgopolov and V G Peschansky for valuable remarks concerning the review. The author is grateful to M A Harutunian, V V Bondarev, W M MacInnes, R Stubi, P-A Probst, B Collet, K Saermark, J Lebech, C K Bak, and J van der Maas for their collaboration. The study was supported by the Russian Academy of Sciences (program: Actual Problems of Low-Temperature Physics of the Presidium of the Russian Academy of Sciences) and by the Russian Foundation for Basic Research (project 14-02-00462). Part of the studies carried out at the Institut de Physique Experimentale, Université de Lausanne, Switzerland) was supported by the Swiss National Foundation for Scientific Research); the author expresses his deep gratitude to these organizations.

References

1. Cracknell A P *Adv. Phys.* **18** 681 (1969)
2. Cracknell A P, Wong K C *The Fermi Surface. Its Concept, Determination and Use in the Physics of Metals* (Oxford: Oxford Univ. Press, 1973)
3. Gantmakher V F *Prog. Low. Temp. Phys.* **5** 181 (1967)
4. Gantmakher V F *Rep. Prog. Phys.* **37** 317 (1974)
5. Kaner E A, Gantmakher V F *Sov. Phys. Usp.* **11** 81 (1968); *Usp. Fiz. Nauk* **94** 193 (1968)
6. Khaikin M S *Adv. Phys.* **18** 1 (1969)
7. Khaikin M S *Sov. Phys. Usp.* **11** 785 (1969); *Usp. Fiz. Nauk* **96** 409 (1968)
8. Édel'man V S *Adv. Phys.* **25** 555 (1976)
9. Edel'man V S *Sov. Phys. Usp.* **20** 819 (1977); *Usp. Fiz. Nauk* **123** 257 (1977)
10. Springford M *Adv. Phys.* **20** 493 (1971)
11. Doezema R E, Koch J F *Phys. Condensed Matter.* **19** 17 (1975)
12. Wagner D K, Bowers R *Adv. Phys.* **27** 651 (1978)
13. Gasparov V A, Huguenin R *Adv. Phys.* **42** 393 (1993)
14. Lee M J G *Phys. Rev.* **187** 901 (1969)
15. Damascelli A, Hussain Z, Shen Z-X *Rev. Mod. Phys.* **75** 473 (2003)
16. Kordyuk A A *Low Temp. Phys.* **40** 286 (2014); *Fiz. Nizk. Temp.* **40** 375 (2014)
17. Kordyuk A A, Borisenko S V *Low Temp. Phys.* **32** 298 (2006); *Fiz. Nizk. Temp.* **32** 401 (2006)
18. Khaikin M S *Sov. Phys. JETP* **14** 1260 (1962); *Zh. Eksp. Teor. Fiz.* **41** 1773 (1961)
19. Khaikin M S *Sov. Phys. JETP* **16** 42 (1963); *Zh. Eksp. Teor. Fiz.* **43** 59 (1962)
20. Mina R T, Khaikin M S *Sov. Phys. JETP* **21** 75 (1965); *Zh. Eksp. Teor. Fiz.* **48** 111 (1965)
21. Mina R T, Edel'man V S, Khaikin M S *Sov. Phys. JETP* **24** 920 (1967); *Zh. Eksp. Teor. Fiz.* **51** 1363 (1966)
22. Khaikin M S, Mina R T *Sov. Phys. JETP* **15** 24 (1962); *Zh. Eksp. Teor. Fiz.* **42** 35 (1962)
23. Gantmakher V F *Sov. Phys. JETP* **15** 982 (1962); *Zh. Eksp. Teor. Fiz.* **42** 1416 (1962)
24. Gantmakher V F *Sov. Phys. JETP* **17** 549 (1963); *Zh. Eksp. Teor. Fiz.* **44** 811 (1963)
25. Gantmakher V F *Sov. Phys. JETP* **19** 1366 (1964); *Zh. Eksp. Teor. Fiz.* **46** 1366 (1963)
26. Gantmakher V F *Sov. Phys. JETP* **16** 247 (1963); *Zh. Eksp. Teor. Fiz.* **43** 345 (1962)
27. Kaner É A *Sov. Phys. JETP* **17** 700 (1963); *Zh. Eksp. Teor. Fiz.* **44** 1036 (1963)
28. Peschansky V G et al. *Physica B+C* **108** 889 (1981)
29. Gasparov V A *Sov. Phys. JETP* **41** 1129 (1975); *Zh. Eksp. Teor. Fiz.* **68** 2259 (1975)
30. Krylov I P, Gantmakher V F *Sov. Phys. JETP* **24** 492 (1967); *Zh. Eksp. Teor. Fiz.* **51** 740 (1966)
31. Gasparov V A, Harutunian M H *Phys. Status Solidi B* **93** 403 (1979)
32. Gasparov V A, Harutunian M H *Phys. Status Solidi B* **74** K107 (1976)
33. Gantmakher V F, Gasparov V A *Sov. Phys. JETP* **37** 864 (1973); *Zh. Eksp. Teor. Fiz.* **64** 1712 (1973)
34. Halse M R *Phil. Trans. R. Soc. A* **265** 507 (1969)
35. Christensen N E, Int. Reprint Physics Lab. I (Lyngby: Technical Univ. of Denmark, 1970)
36. MacInnes W M et al., in *Recent Developments in Condensed Matter Physics* Vol. 2 *Metals, Disordered Systems, Surfaces, and Interfaces* (Ed. J Devrees) (Berlin: Springer, 1981) p. 25
37. Stubi R et al. *Jpn. J. Appl. Phys.* **26** 643 (1987)
38. Stubi R, Probst P-A, Huguenin R, Gasparov V A *J. Phys. F* **18** 1211 (1988)
39. Henningsen J O, Falk D S *Phys. Rev. Lett.* **26** 1174 (1971)
40. Gantmakher V F, Lebech J, Bak C K *Phys. Rev. B* **20** 5111 (1979)

41. Gasparov V A, Lebech J, Saermark K *J. Low Temp. Phys.* **41** 257 (1980)
42. Gasparov V A, Lebech J, Saermark K *J. Low Temp. Phys.* **50** 379 (1983)
43. Lomer W M *Proc. Phys. Soc. Lond.* **80** 489 (1962)
44. Lomer W M *Proc. Phys. Soc. Lond.* **84** 327 (1964)
45. Boiko V V, Gasparov V A, Gverdtsiteli I G *Sov. Phys. JETP Lett.* **6** 212 (1967); *Pis'ma Zh. Eksp. Teor. Fiz.* **6** 737 (1967)
46. Boiko V V, Gasparov V A, Gverdtsiteli I G *Sov. Phys. JETP* **29** 267 (1969); *Zh. Eksp. Teor. Fiz.* **56** 489 (1969)
47. Boiko V V, Gasparov V A *Sov. Phys. JETP* **34** 1266 (1972); *Zh. Eksp. Teor. Fiz.* **61** 2362 (1972)
48. Boiko V V, Gasparov V A *Sov. Phys. JETP* **34** 1054 (1972); *Zh. Eksp. Teor. Fiz.* **6**1 1976 (1972)
49. Boiko V V, Gasparov V A *Metallofizika* **37** 11 (1971)
50. Boiko V V, Gasparov V A *Sov. Phys. Solid State* **12** 254 (1970); *Fiz. Tverd. Tela* **12** 310 (1970)
51. Arutunyan M A, Gantmakher V F, Gasparov V A *Izv. Akad. Nauk Arm. SSR*: *Fiz.* **13** 474 (1978)
52. Boiko V V, Gantmakher V F, Gasparov V A *Sov. Phys. JETP* **38** 604 (1974); *Zh. Eksp. Teor. Fiz.* **65** 1219 (1973)
53. van der Maas J, Huguenin R, Gasparov V A *J. Phys. F* **15** L271 (1985)
54. Gantmakher V F, Krylov I P *Sov. Phys. JETP* **20** 1418 (1965); *Zh. Eksp. Teor. Fiz.* **47** 2111 (1964)
55. Gantmakher V F, Krylov I P *Sov. Phys. JETP* **22** 734 (1966); *Zh. Eksp. Teor. Fiz.* **49** 1054 (1966)
56. Gantmakher V F, Kaner E A *Sov. Phys. JETP* **21** 1053 (1965); *Zh. Eksp. Teor. Fiz.* **48** 1572 (1965)
57. Mar'yakhin A A, Naberezhnykh V P *JETP Lett.* **3** 130 (1966); *Pis'ma Zh. Eksp. Teor. Fiz.* **3** 205 (1966)
58. Naberezhnykh V P, Tsymbal L T *JETP Lett.* **5** 263 (1967); *Pis'ma Zh. Eksp. Teor. Fiz.* **5** 319 (1967)
59. Jaquier A et al. *J. Phys. Condens. Matter* **3** 10065 (1991)
60. MacInnes W M et al. *J. Phys. F* **7** 655 (1977)
61. Price P J *IBM J. Res. Develop.* **4** 152 (1960)
62. Lur'e M A, Peschansky V G, Yiasemides K *J. Low Temp. Phys.* **56** 277 (1984)
63. Okulov V I, Ustinov V V *Sov. Phys. JETP* **40** 584 (1975); *Zh. Eksp. Teor. Fiz.* **67** 1176 (1974)
64. Ustinov V V *Phys. Metals Metallogr.* **52** (4) 27 (1981); *Fiz. Met. Metalloved.* **52** 709 (1981)
65. Peschanskii V G, Yiasemides K *Sov. J. Low Temp. Phys.* **6** 260 (1980); *Fiz. Nizk. Temp.* **6** 541 (1980)
66. Bondarev V V, Gasparov V A *JETP Lett.* **41** 175 (1985); *Pis'ma Zh. Eksp. Teor. Fiz.* **41** 143 (1985)
67. Tsoi V S, Razgonov I I *Sov. Phys. JETP* **74** 597 (1978); *Zh. Eksp. Teor. Fiz.* **74** 1137 (1978)
68. Tsoi V S, in *Soviet Scientific Review Section A Phys. Rev.* Vol. 2 (Ed. I M Khalatnikov) (London: Harwood Acad., 1980) p. 395
69. Gantmakher V F, Dolgopolov V T *Sov. Phys. JETP* **33** 1215 (1971); *Zh. Eksp. Teor. Fiz.* **60** 2260 (1971)
70. Gantmakher V F, Dolgopolov V T *Sov. Phys. JETP* **33** 1215 (1971); *Zh. Eksp. Teor. Fiz.* **66** 1461 (1974)
71. Dolgopolov V T *Sov. Phys. Usp.* **23** 134 (1980); *Usp. Fiz. Nauk* **130** 241 (1980)
72. Dolgopolov V T, Murzin S S *Sov. Phys. JETP Lett.* **23** 190 (1976); *Pis'ma Zh. Eksp. Teor. Fiz.* **23** 213 (1976)
73. Babkin G I, Dolgopolov V T, Chuprov P N *Sov. Phys. JETP* **48** 907 (1978); *Zh. Eksp. Teor. Fiz.* **75** 1801 (1978)
74. Dolgopolov V T, Murzin S S, Chuprov P N *Sov. Phys. JETP* **51** 166 (1980); *Zh. Eksp. Teor. Fiz.* **78** 331 (1980)
75. Murzin S S, Dolgopolov V T *Sov. Phys. JETP* **52** 1155 (1980); *Zh. Eksp. Teor. Fiz.* **79** 2282 (1980)
76. Lifshits I M, Azbel M Ya, Kaganov M I *Electron Theory of Metals* (New York: Consultants Bureau, 1973); Translated from Russian: *Elektronnaya Teoriya Metallov* (Moscow: Nauka, 1971)
77. Gasparov V A et al. *Phys. Rev. Lett.* **101** 097006 (2008)
78. Kramer R B G et al. *Phys. Rev. Lett.* **95** 267209 (2005)
79. Kramer R B G et al. *Phys. Rev. B* **82** 075101 (2010)
80. Doiron-Leyraud N et al. *Nature* **447** 565 (2007)
81. Vignolle B et al. *Nature* **455** 952 (2008)
82. Bangura A F et al. *Phys. Rev. Lett.* **100** 047004 (2008)
83. Hossain M A et al. *Nature Phys.* **4** 527 (2008)
84. Jaudet C et al. *Phys. Rev. Lett.* **100** 187005 (2008)
85. Audouard A et al. *Phys. Rev. Lett.* **103** 157003 (2009)
86. Singleton J et al. *Phys. Rev. Lett.* **104** 086403 (2010)
87. Vignolle B et al. *Phys. Rev. B* **85** 224524 (2012)
88. Sebastian S E, Harrison N, Lonzarich G G *Rep. Prog. Phys.* **75** 102501 (2012)
89. Barišiś N et al. *Nature Phys.* **9** 761 (2013)
90. Doiron-Leyraud N et al. *Nature Commun.* **6** 6034 (2015)
91. Sebastian S E, Proust C *Annu. Rev. Condens. Matter Phys.* **6** 411 (2015); arXiv:1507.01315
92. Zabolotnyy V B et al. *Phys. Rev. B* **76** 024502 (2007)